Quadrupole-Enhanced Raman Scattering
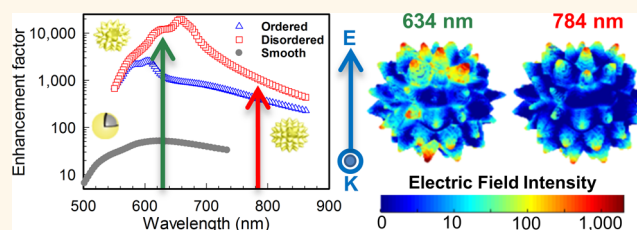
Simon P. Hastings,[†,‡] Pattanawit Swanglap,[§,#] Zhaoxia Qian,[‡] Ying Fang,[§] So-Jung Park,[‡,⊥,*] Stephan Link,[§] Nader Engheta,[†,‖] and Zahra Fakhraai[‡,*]

[†]Department of Physics, University of Pennsylvania, Philadelphia, Pennsylvania 19104, United States, [‡]Department of Chemistry, University of Pennsylvania, Philadelphia, Pennsylvania 19104, United States, [§]Department of Chemistry, Rice University, Houston, Texas 77005, United States, [⊥]Department of Chemistry and Nano Science, Global Top 5 Program, Ewha Womans University, 52 Ewhayeodae-gil, Seodaemun-gu, Seoul 120-750, Korea, and [‖]Department of Electrical and Systems Engineering, University of Pennsylvania, Philadelphia, Pennsylvania 19104, United States. [#]Present address: Department of Chemistry, Silpakorn University, Nakhon Pathom, Thailand.

ABSTRACT Dark, nonradiating plasmonic modes are important in the Raman enhancement efficiency of nanostructures. However, it is challenging to engineer such hotspots with predictable enhancement efficiency through synthesis routes. Here, we demonstrate that spiky nanoshells have designable quadrupole resonances that efficiently enhance Raman scattering with unprecedented reproducibility on the single particle level. The efficiency and reproducibility

of Quadrupole Enhanced Raman Scattering (QERS) is due to their heterogeneous structure, which broadens the quadrupole resonance both spatially and spectrally. This spectral breadth allows for simultaneous enhancement of both the excitation and Stokes frequencies. The quadrupole resonance can be tuned by simple modifications of the nanoshell geometry. The combination of tunability, high efficiency, and reproducibility makes these nanoshells an excellent candidate for applications such as biosensing, nanoantennaes, and photovoltaics.

KEYWORDS: SERS · spiky nanoshells · QERS · quadrupole resonance · plasmon resonance · Raman spectroscopy

Surface enhanced Raman spectroscopy (SERS)[1] has been widely studied for its diverse potential applications ranging from chemical[2−5] and biological[6−8] detection to intracellular imaging[9] and medicine.[10] When a Raman analyte is placed in the near-field of a plasmonic nanostructure, the vibrational modes of the analyte couple to the local electric field, and the Raman scattering cross section scales with the local electric field to the fourth power.[11] As such, SERS substrates are often designed to generate hotspots at sharp corners or small gaps, either between nanostructures[3,12−15] or engineered into single nanoparticles.[16−18] While hotspots in particle junctions can be used to achieve extremely high SERS cross sections, they are difficult to engineer,[19] and it is challenging to precisely place the analyte in the right position and orientation for maximum coupling. Furthermore, the enhancement is extremely sensitive to small changes in the local structure including the size of the gap,[19] the polarization of the incident light,[20] and the direction of detection.[21] These factors lead to extremely large

variations of SERS intensity in hotspot-based SERS substrates.

In contrast, in simple single nanoparticles such as isolated spheres and rods, the near-field intensity is usually dominated by the dipolar resonance of the localized surface plasmon resonance (LSPR).[22] Thus, SERS enhancement on these simple nanoparticles usually correlates well with far-field plasmon resonances. However, the enhancement factors on these simple nanoparticles are much lower than hotspot based substrates. In nonspherical or large nanostructures, a higher order resonance called the quadrupole resonance can occur and can lead to SERS enhancement due to bright quadrupole resonances.[17,23] In smaller nanoparticles, the quadrupole resonances are dark and their electric fields decay rapidly with distance from the particle. However, they can still have a significant contribution to the near-field intensity.[24−26]

Here, we demonstrate both experimentally and theoretically that dark quadrupole resonances can play an important role in the SERS cross section, and thereby achieve

©2014 American Chemical Society

highly efficient and uniform SERS enhancement. We have recently developed a new method of synthesis to produce highly structured metal nanoshells composed of numerous sharp spikes called spiky nanoshells.[27−29] These nanoshells were shown to be remarkably effective SERS substrates with exceptionally reproducible Raman scattering signals on the single particle level.[28] In this manuscript, we demonstrate that Raman scattering with even larger cross section and narrower distribution can be achieved by excitation at the quadrupole resonance, and that the remarkable reproducibility results from the disorder in the spiky nanoshells that broadens the quadrupole resonance. The disorder in the structure results in the formation of spatially delocalized hotspots on the tip of many spikes that can enhance the Raman cross section of randomly placed analyte molecules. This is in sharp contrast with other observations of SERS enhancement in hotspots, where the direction of the detection and the exact position of the analyte are extremely important and with particular detection methods such as directivity enhanced Raman scattering (DERS) where the plasmonic structure itself has a preferred direction to its Raman cross section.[21]

RESULTS AND DISCUSSION

For this study, spiky gold nanoshells were synthesized by surfactant-assisted seed growth method[27−29] and characterized by UV−vis absorption spectroscopy, transmission electron microscopy (TEM), and scanning electron microscopy (SEM). Figure 1a shows an SEM image of the spiky nanoshells used in this study. Single particle dark-field backscattering (Figure 1d,f) and Raman spectroscopy (Figure 1g) were performed on individual spiky nanoshells immobilized on a glass substrate and coated with 4-mercaptobenzoic acid (Figure 1b). They were then studied with an inverted microscope (Figure 1c) to examine how the far-field backscattering characteristics correlate with the Raman scattering cross section. Ensemble averaged spectra and histograms of these data are shown in Supporting Information Figure S1, with additional backscattering spectra in Supporting Information Figure S2. SERS spectra were collected at 633 and 785 nm excitation wavelengths. After all optical measurements, the nanoshell samples were imaged by SEM (Figure 1e) to make sure that only single particle data are included in the data analyses, as the variable shape
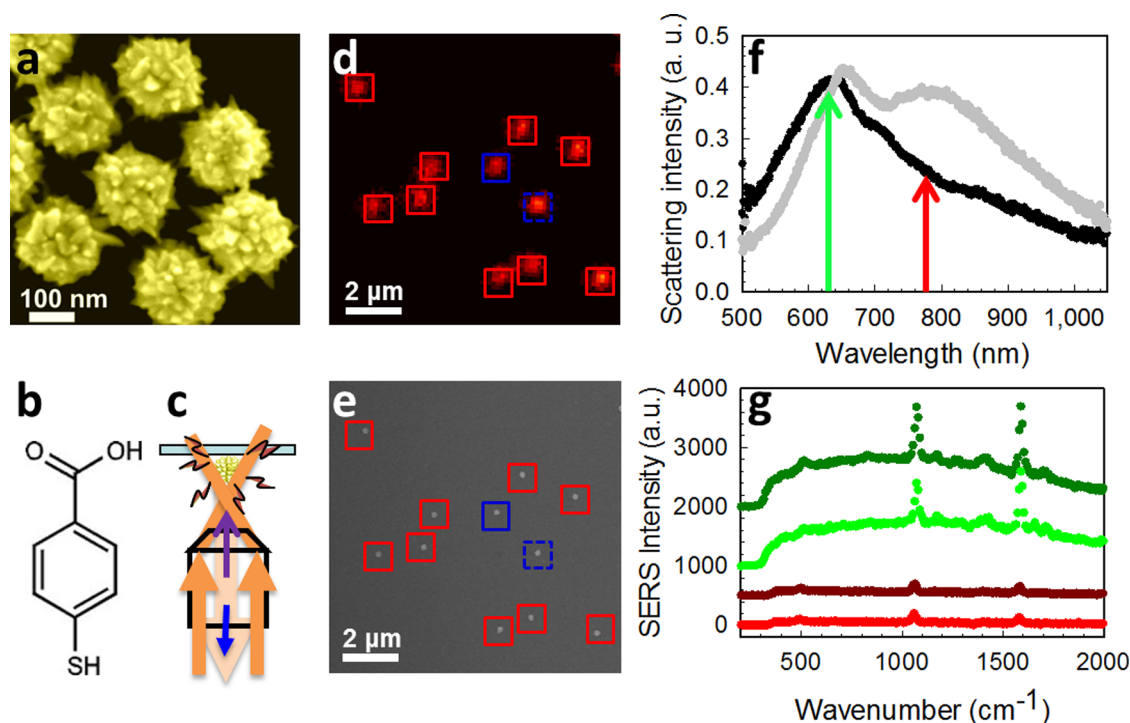

Figure 1. SERS and dark-field scattering measurements and apparatus. (a) An SEM image of a collection of spiky nanoshells. (b) The structure of 4-mercaptobenzoic acid that was used as the Raman analyte. (c) Schematic of the single particle backscattering and Raman scattering measurements. Orange arrows show the direction of incident and backscattered white light, while the purple and blue arrows indicate the orientation of the laser excitation and the Stokes lines, respectively. (d) Dark-field backscattering image of spiky nanoshells. (e) SEM image of the same area as (d) used to ensure that only single particle spectra were collected. Boxes are added to individual spiky nanoshells to aid in the comparison of the images. (f) Representative examples of typical dark-field scattering spectra from the two particles highlighted with blue boxes. Green and red arrows show the excitation wavelengths used for Raman scattering. (g) SERS spectra at 633 nm (green), and 785 nm (red) excitations. The dark green and dark red SERS spectra represent spectra obtained from the particle with the solid black far-field scattering spectrum in (f), and highlighted by the solid blue boxes in (d) and (e), and the light green and light red SERS spectra correspond to the single particle spectrum given by the gray far-field scattering spectrum, shown in the dashed blue boxes in (d) and (e). The dark red, light green, and dark green spectra are shifted vertically by 500, 1000, and 2000 intensity units, respectively, for better visualization.
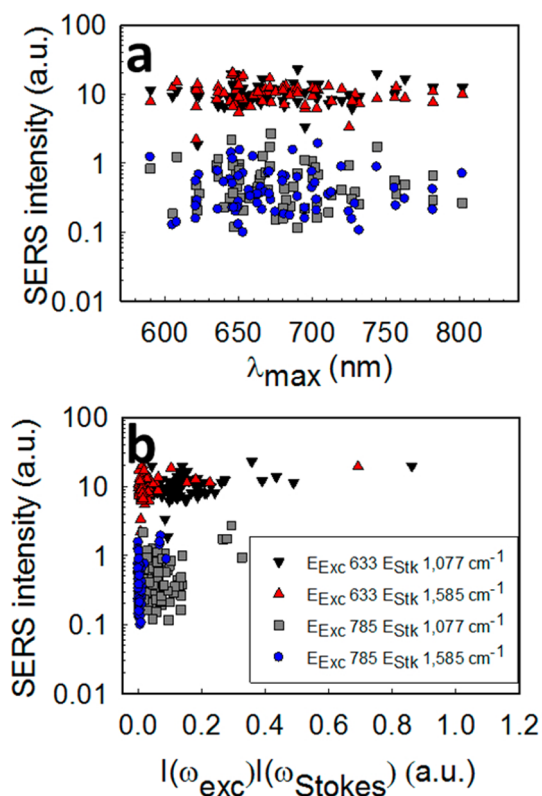
Figure 2. Single particle SERS and dark-field scattering correlations. (a) Correlation between the measured SERS intensity and the peak backscattering wavelength (λ_{max}) for 633 excitation with 1077 cm^{-1} Stokes scattering (black downward triangles), 1585 cm^{-1} Stokes scattering (red upward triangles), 785 excitation with 1077 cm^{-1} Stokes scattering (gray squares), and 1585 cm^{-1} Stokes scattering (blue circles). (b) Correlation between Raman signal intensity and the calculated enhancement factors based on the far-field scattering spectrum for the same data in a.

of the backscattering spectra did not allow for conclusive identifications of isolated nanoshells. Representative SERS spectra are shown in Figure 1g. More details of the sample preparation and Raman experiments can be found in the Supporting Information.[30]

SERS intensity changes significantly with the excitation wavelength. As shown in Figure 2, for all 71 particles examined, the Raman intensity at 633 nm was about a factor of 20 higher compared to the 785 nm excitation for both 1585 and 1077 cm^{-1} peaks. In addition, at 633 nm excitation the Raman signals show significantly lower intensity variations compared to those at 785 nm, with 34% and 80% standard deviations, respectively. Note that the signal is remarkably more reproducible for both wavelengths when compared to intensity variations found for nanoparticle dimers, in which the enhancement factor can vary by 4 orders of magnitude depending on the interparticle distance.[15]

Figure 2 shows the intensity of each Raman line of the analyte, measured at both excitations as a function of peak far-field wavelength (λ_{max}) and the calculated

enhancement factor as described below. The correlation plots in Figure 2 show that the measured SERS intensity is neither correlated with the far-field scattering peak of the nanoshells (Figure 2a), nor with the enhancement factor calculated based on the far-field spectrum (Figure 2b). Single particle measurements also show that the presence of an apparent dip, which was sometimes observed at longer wavelengths (gray spectrum in Figure 1f), did not visibly affect the SERS intensities on a single particle level. As the SEM image in Figure 1e shows, the particles are well separated and the backscattering feature shown in Figures 1f and S2 cannot be the result of interference between two nearby particles. The origin of this behavior will be discussed in a future manuscript. Therefore, far-field spectral features can neither explain the origin of the strong enhancement factors at 633 nm excitation compared to the 785 nm excitation, nor its exceptional reproducibility. Therefore, specific near-field effects must be considered in order to explain these experimental observations.

To explore the origin of the strong relative Raman enhancement at 633 nm, it is necessary to examine the underlying mechanisms of SERS. The Raman scattering dipole of an analyte, μ_α, placed in an electrical field can be described as[31]

$$\mu_\alpha = \alpha_{\alpha\beta}E_\beta + \frac{1}{3}A_{\alpha\beta\gamma}E_{\beta\gamma} + \dots \qquad (1)$$

In this equation $\alpha_{\alpha\beta}$ and $A_{\alpha\beta\gamma}$ are the dipole and quadrupole polarizability tensors of the molecule, E_β is the electric field, and $E_{\beta\gamma}$ is the electric field gradient with respect to γ, where α, β, and γ denote the coordinates. Higher order terms are assumed to be small and are ignored. The analyte used in this study, 4-mercaptobenzoic acid, has two vibrational bands in the experimental window as shown in Figure 1g. Both vibrational bands are dipolar in nature, and therefore, the second term in eq 1 is negligible (details provided in the Supporting Information[30]). Under these conditions, the nonresonant SERS enhancement factor (EF) can be described by[11,32,33]

$$EF = \frac{I_{Exc}I_{Stokes}}{I_0^2} \qquad (2)$$

where I_{Exc} is the electric field intensity at the excitation wavelength, I_{Stokes} is the near-field electric field intensity at the Stokes wavelength, and I_0^2 is the near-field electric field intensity of the incident wave to the power of two.

As mentioned above, in simple nanoparticles, where both near-field and far-field electric fields can be described by a dipole moment, the far-field spectrum provides a reasonable guide for predicting and optimizing the Raman enhancement factor.[11] However, in nanostructures containing hotspots,[14,15] the enhancement factors are often uncorrelated with the far-field
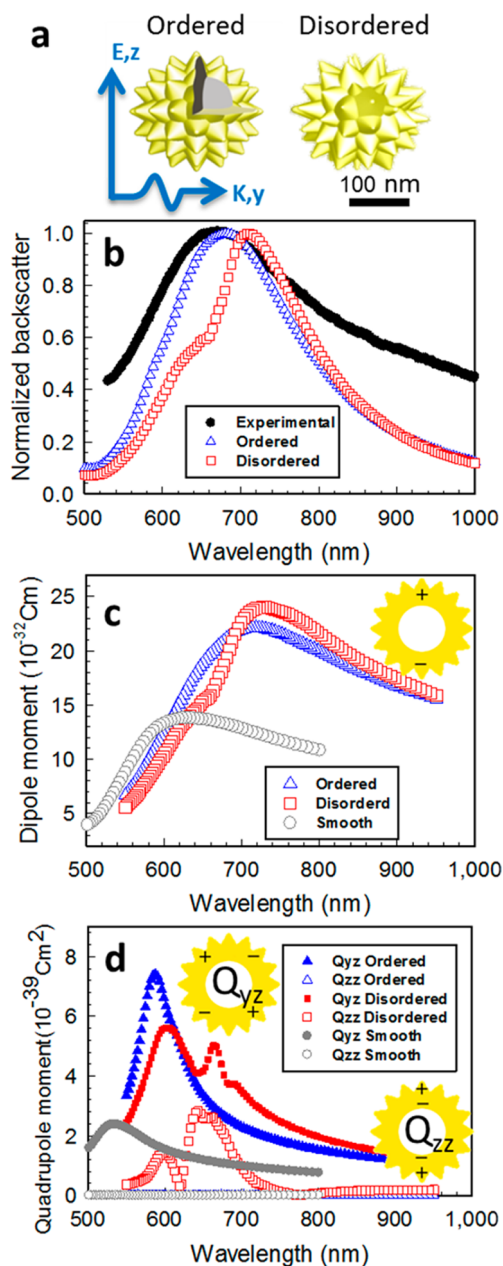
Figure 3. Simulated far-field and multipole spectra for spiky nanoshells. (a) Modeled structures of spiky nanoshells. The simplified ordered nanoshell is shown on the left, and the disordered structure is shown on the right. A scale bar indicates the approximate scale of the nanoshells. Part of the ordered nanoshell is removed to show the polystyrene core present in both models. Please see the Methods and Supporting Information[30] for more details. (b) Ensemble averaged experimental dark-field backscattering spectrum (black) compared with the simulated far-field backscattering spectra of the ordered (blue) and disordered (red) model nanoshells. (c) Electric dipole moment of the ordered (blue) and disordered (red) nanoshells compared with a smooth nanoshell (gray) with the same amount of gold as the disordered nanoshells and the same core size. (d) Electric quadrupole moments of the ordered (blue), disordered (red), and smooth (gray) nanoshells. Solid symbols indicate the quadrupole moment in the yz direction, while the open symbols show the quadrupole moment in the zz direction. The y and z directions denote the direction of propagation and polarization vectors of the incident wave in the Cartesian coordinates. All higher moments are orders of magnitude weaker.
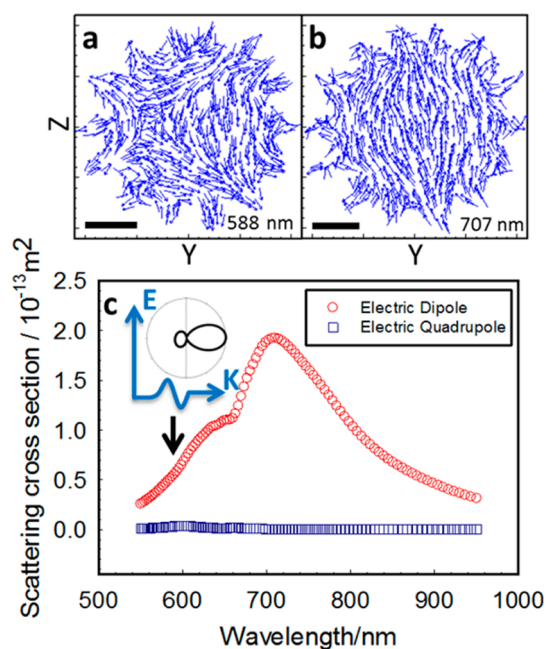

Figure 4. Far-field and near-field response of the dipole and quadrupole modes. (a) Polarization currents in the disordered spiky nanoshell obtained from the FDTD simulation at 588 nm (the Q_{yz} quadrupole resonance), projected onto the yz plane. Magnitude was removed to produce uniform vector lengths. (b) Polarization currents of the same structure at 707 nm (the dipole resonance). The scale bars are 50 nm in length for both (a) and (b). (c) Calculated scattering cross section of the dipole (red) and quadrupole (blue) modes. Inset shows the far-field angular distribution at the yz quadrupole peak (588 nm), which is clearly dipolar in nature. The y and z directions denote the direction of propagation and polarization vectors of the incident wave in the Cartesian coordinates.

spectral features. Wustholz et al.[15] showed that in these cases the optimum frequency for SERS enhancement can be predicted through detailed understanding, via simulation, of the near-field around the nanoparticle.

Near-field profiles of spiky nanoshells were obtained by Finite-Difference Time Domain (FDTD) simulations using the two models shown in Figure 3a. As in previous studies,[28,29] these models were built based on experimentally relevant parameters (see Supporting Information[30]) in order to elucidate the structural origin of the unusual excitation wavelength dependence of the SERS intensities. Ordered and disordered structures were created to explore the heterogeneity of the actual nanoshells, which was found to play an important role in the uniform SERS intensity (vide infra). The calculated backscattering (Figure 3b) and extinction (Supporting Information Figure S3) spectra of these models match well with the experimentally measured spectra (see Supporting Information[30]). This provides confidence that the modeled structures are good representations of typical spiky nanoshells. To avoid bias from the randomization, 10 additional rerandomized structures were studied as shown in Supporting Information Figure S4. The dipole and

quadrupole moments of these model nanoshells were calculated from the polarization currents, using the following equations:[34]

$$\vec{p} = \frac{i}{\omega} \int \vec{J}(\vec{r}') \, dV' \tag{3}$$

$$Q_{\alpha\beta} = \frac{i}{\omega} \int J_\alpha(\vec{r}')\vec{r}'_\beta + J_\beta(\vec{r}')\vec{r}'_\alpha \, dV' \tag{4}$$

In these equations, $\vec{p}$ is the dipole moment vector, Q is the quadrupole moment tensor, $\vec{J}$ is the polarization current volume density, $\vec{r}'$ is the position vector, and ω is the angular frequency of excitation where the time harmonic wave, $\exp(-i\omega t)$, has been considered. α and β each denote x, y or z depending on which quadrupole moment is calculated. Here y denotes the direction of propagation and z corresponds to the direction of polarization of the incident field. The integral is over the entire simulation space. Calculated spectral shapes of the dipole and quadrupole moments for the two structures are presented in Figures 3c,d, exhibiting strong quadrupole resonances. For comparison, we provide the same results for a smooth shell with gold volume equal to the disordered model. The polarization current maps at the Q_{yz} quadrupole and the dipole resonances are shown in Figures 4, panels a and b, respectively, for the disordered model, and in Supporting Information Figure S5 for the ordered model. These current maps show that despite significant disorder and numerous sharp points in the nanoshell structure, the polarization current, and the local electric fields are primarily dominated by the particular quadrupole or dipole resonance at a given frequency.

To demonstrate that the quadrupole mode can be considered a dark mode in the far-field, the scattering cross section of the dipole and quadrupole modes were calculated for the disordered nanoshell. This is performed assuming that there was no mixing or interference between the modes. We note that given the fine features in the far-field scattering spectrum as shown in Figure 3b and in the experimental data of Figures 1f and S2, modal interference is possible. The details of this phenomenon are beyond the scope of this paper and will be discussed in a separate publication, where we show the coupling is less than about 5% and can be ignored for the purposes of this paper. Figure 4c shows that the quadrupole mode is indeed a dark mode in the far-field and does not significantly contribute to the far-field scattering cross section (see Supporting Information[30] for details of the calculation). The inset of Figure 4c and additional polar plots presented in Supporting Information Figure S6 also confirm that the angular distribution of the far-field scattering follows the dipolar angular distribution at both the dipole and quadrupole resonance wavelengths with no additional lobes or substantial changes

to the nodal plane as seen in directional emission.[35] Furthermore, the addition of disorder to the structure does not significantly change the far-field LSPR peak (Figure 3b) or the dipole resonance (Figure 3c) except for potential interference between the Q_{zz} quadrupole and the dipole, which results in a small apparent shift in the dipole resonance peak.

While the addition of disorder to the structure does not significantly change the far-field LSPR peak or the dipole resonance, it strongly affects the quadrupole resonances (Figure 3d). In the smooth nanoshell and in the ordered structure, the only nonzero quadrupole moment is in the yz plane (Q_{yz}), where y and z denote the direction of propagation and the polarization of the incident wave, respectively. In contrast, in the disordered structure, which more closely represents the imperfect structure of the synthesized spiky nanoshells, nonuniform spike lengths generate additional nonzero quadrupoles with the strongest in the polarization direction (Q_{zz}). In comparison to the smooth shells, the quadrupole resonances are nearly a factor of 4 stronger and are spectrally much broader.

As shown in Figure 3d, compared to the ordered nanoshell, the disordered nanoshell has spectrally broadened quadrupole resonances with more spectral features (examples from more nanoshell realizations are shown in Supporting Information Figure S4 and averages in Supporting Information Figure S7). This is achieved without a significant change in the peak amplitude or the quality factor (QF = $f/\delta f$, where f is the frequency). The spectral breadth of the quadrupole resonance in the disordered structure enables efficient enhancement of the electric field both at the excitation and the Stokes scattering frequencies and is crucial to the experimental observation of Quadrupole Enhanced Raman Scattering (QERS). We note that the fine features in the disordered structure depend on the details of the randomization and vary from one model to another. Supporting Information Figures S4 and S7 show that despite these variations the conclusions stated here remain valid for an ensemble of disordered nanoshells.

The electric field intensity and the corresponding near-field enhancement factors (based on eq 2) can be directly calculated using the results of the FDTD simulations. To perform these calculations, the electric field intensity and the enhancement factors were integrated inside a shell of thickness 2.1 nm around the surface of each nanostructure (see Supporting Information[30] for more details). Figure 5a shows that the incoming electric field intensity is most strongly enhanced at the Q_{yz} resonance in the ordered nanoshell, and at the Q_{zz} resonance in the disordered nanoshell. In contrast, for the smooth nanoshell the maximum intensity occurs at the dipole resonance. The Raman enhancement factors (Figure 5b and Supporting Information Figures S8 and S4), as determined
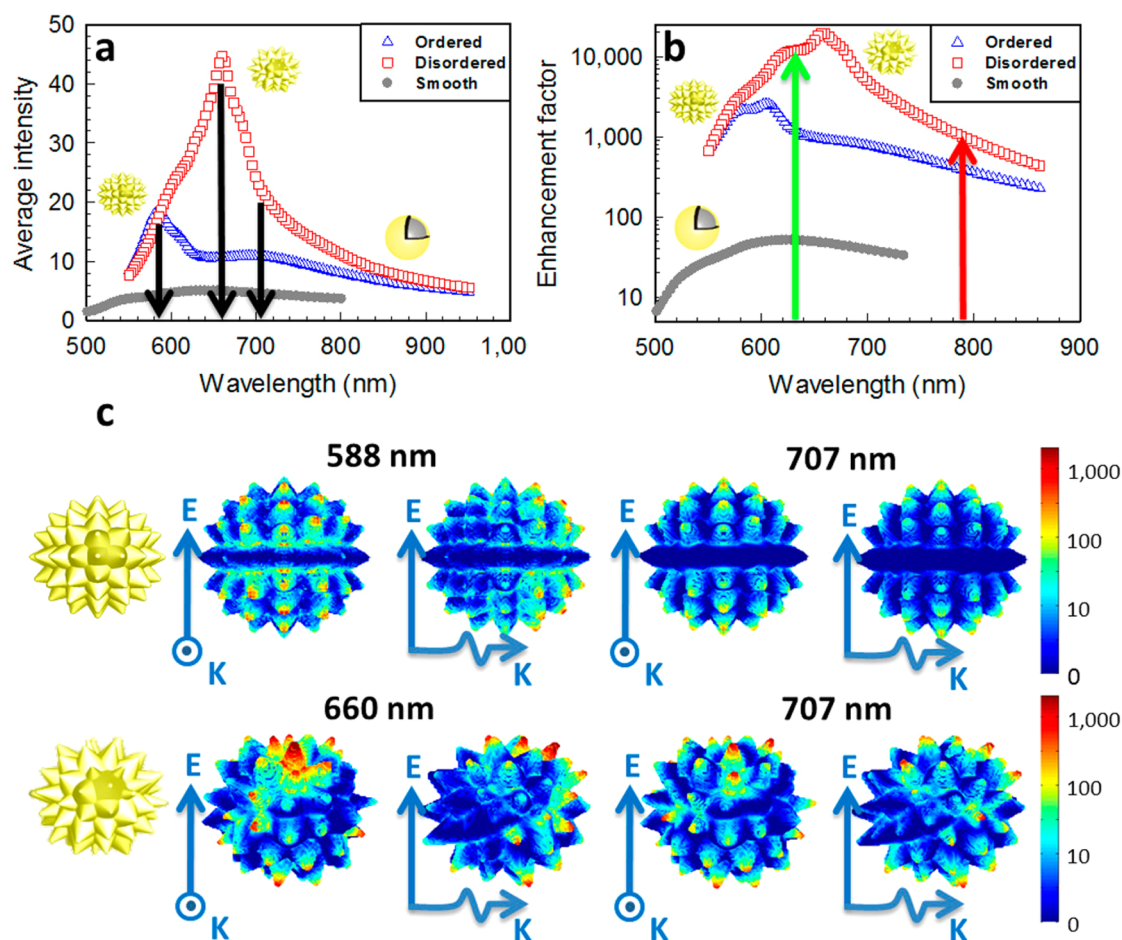
Figure 5. Simulated near-field enhancement of spiky nanoshells. (a) Integrated electric field intensity in a volume within 2.1 nm of the surface of the ordered (blue), the disordered (red), and the smooth nanoshells (gray), normalized to a unit incident electric field. (b) Raman enhancement factors calculated for the 1077 cm^{-1} Stokes line based on the near-field intensities. The green and red arrows show the laser excitation wavelengths. (c) Electric field intensity maps (log scale) of the ordered (top row) and disordered (bottom row) nanoshells. These maps were generated at the wavelength of the peak average intensity for each structure, 588 nm for the ordered nanoshell, and 660 nm for the disordered nanoshell and the dipole peak at 707 nm. Black arrows in (a) show the three wavelengths at which these plots are generated. Note that disorder delocalizes the hotspots.

based on eq 2, are stronger and broader in the disordered structure compared to those of the ordered structure and the smooth nanoshell. Additionally, unlike the smooth nanoshell, in both ordered and disordered nanoshells the Raman enhancement factor is dominated by the quadrupole resonance rather than the dipole resonance. Furthermore, the maximum enhancement factors are at least 2 orders of magnitude higher than the enhancement factor in the smooth nanoshell. It is important to note that the real experimental enhancement factors may be even larger than these calculations because the real nanoshells have more sharp points, fine edges, long spikes, and other small-scale structures than the modeled particles, which would most likely further increase the QERS signal (see the Supporting Information[30] for more details).

Supporting Information Figure S4 shows similar results for 10 different randomized structures and shows that the choice of the particular randomization does not affect these conclusions. Furthermore, this figure shows that while the addition of disorder significantly affects the detailed structure of the quadrupole resonances, the collective effect of all these resonances lead to an emerging enhancement factor with significantly smaller variations. On the basis of these calculations, the Raman enhancement due to near-field enhancement at 633 nm (green arrow in Figure 5b) is a factor of 11.2 larger than the Raman enhancement at 785 nm (red arrow in Figure 5b) for the disordered particle shown in Figure 5b. The average ratio of enhancement is 6.8 for the ensemble of particles shown in Supporting Information Figure S4b. It is necessary to also consider the λ^{-4} wavelength dependence of the Raman cross section,[36] which contributes an additional factor of 2.5 to the total relative enhancement between the two excitation wavelengths. The combined relative enhancement factor is on average 17.0, which is in strong agreement with the experimental results of an average enhancement of 17.5 shown in Figure 2. Supporting Information Figure S9

shows the total relative enhancement factor, normalized to the Stokes shift at 633 nm enhancement, factoring in both the wavelength dependence and the near-field enhancement factors for the same structures as the one shown in Figure 5b. This result indicates that the strong and uniform Raman signal from spiky nanoshells is predominantly due to the QERS enhancement at 633 nm. Additionally, the variations of the signal at 633 nm are 15% smaller than those at 785 nm, which is also consistent with the experimental observations of QERS enhancement in single nanoshells as shown in Figure 2.

To understand the origin of the broad, heterogeneous spectral features, we examined the spatial distribution of the electric field intensity. Figure 5c presents electric field intensity maps at various wavelengths for both models (additional field intensity maps for both structures can be found in Supporting Information Figure S10). These calculations show that the electric field intensity is mostly localized at the tip of the spikes and is spatially coupled with the strongest multipole resonance at a given frequency. They also show that the electric field at the tip of the spikes is stronger at the quadrupole resonance of each structure compared to the dipole resonance, explaining the effective increase in the Raman enhancement factors at the quadrupole resonance (Figure 5b). Furthermore, they reveal that the added heterogeneity in the disordered structure spatially delocalizes the field by exciting spikes in previously dark places with stronger intensities than are present in the ordered structure. This is crucial in uniform QERS enhancement observed on a single particle level, because it shows that the specific position and orientation of the analyte is not crucial in coupling with a randomly oriented hotspot. This is in strong contrast with most hotspot based nanostructures, where the direction of detection and the position and orientation of the particle can have an strong influence on the SERS enhancement and specific gap size and shape.

To demonstrate that the hotspots observed in Figure 5c are the result of the quadrupole resonance and not any higher order resonances, spherical harmonic components, which can be directly related to the multipole modes, were calculated on the surface of a sphere just outside of the model nanoshell (more details in Supporting Information[30]). Calculations of the higher order harmonics in Supporting Information Figure S11 show that although these higher-order harmonics contribute to the overall near-field intensity, these contributions are significantly smaller than the first two harmonics, the dipole and the quadrupole. The small intensity observed in higher-order harmonics are largely the result of hotspots locally modulating the electric-field, as shown in Figure 5c, and Supporting Information Figures S10 and S12. The higher-order harmonics also do not present any new resonances in these model nanoshells providing strong evidence that the dipole and quadrupole
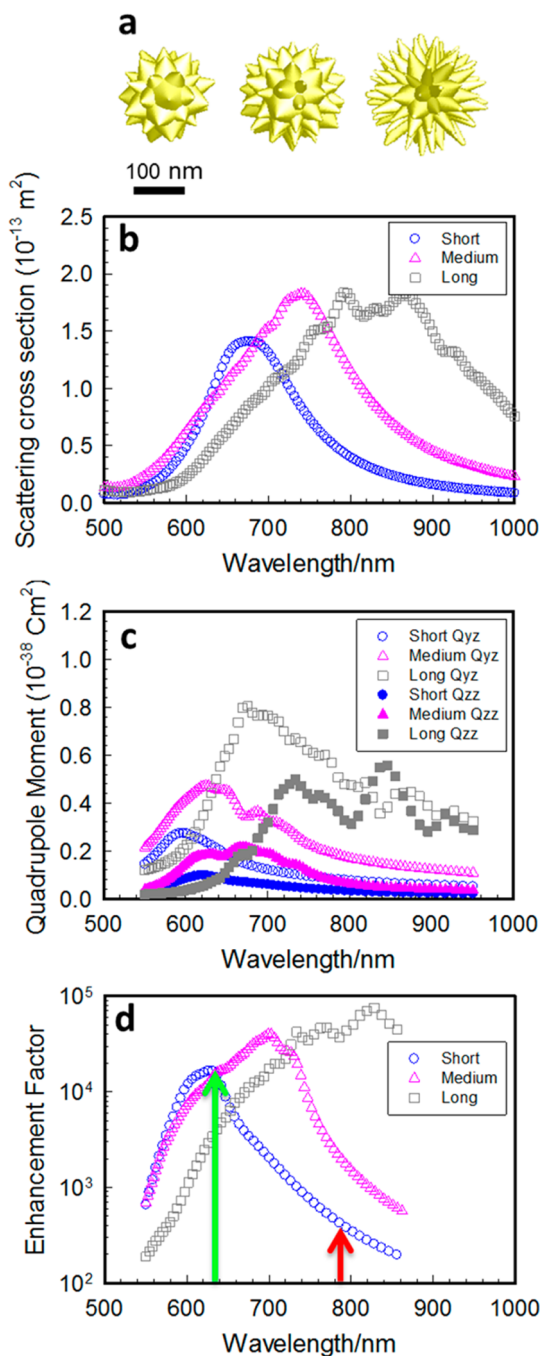

Figure 6. Ensemble-averaged behavior of three families of nanoshells, based on experimentally accessible structures. (a) Representative shapes of three synthesizable nanoshells produced based on our previous work[29] by randomizing the spike parameters (see Supporting Information for details[30]). (b) Average far-field scattering cross section of 10 different realization of each structure. (c) Average Q_{yz} and Q_{zz} quadrupoles for each structure. (d) The average enhancement factor at 1077 cm^{-1}.

resonances dominate the near-field features of the electric field intensity. We can demonstrate the effect of the quadrupole in the exceptional enhancement of the electric field using a simplified model of the spiky nanoshell, as described in an earlier publication.[29] In this structure the spikes were only placed on a

planar geometry as shown in Supporting Information Figure S13. In this model, it is possible to turn the far-field coupling to the quadrupole mode on and off by switching the propagation direction of light with respect to the plane of the spikes, while the dipole moment remains exactly the same in both orientations. Supporting Information Figure S13d shows an increased enhancement due to the quadrupole mode with no corresponding change to the far-field scattering spectrum of the particle. Additionally, Supporting Information Figure S13f shows that the high near-fields present at the spike tips are due to the coupling of the quadrupole resonance with the electric field at the tip of the spikes, and do not represent a separate electromagnetic resonance. This coupling of a core mode to a tip mode has been theoretically predicted in the gold nanostar system.[37]

As shown in our previous work,[29] the synthesis applied to produce spiky nanoshells allows production of highly tunable surface morphologies with tunable far-field scattering cross sections. This tunability can be expanded to the QERS cross section. Figure 6a shows three model structures based on experimentally relevant values of the spiky nanoshells as reported in our previous publication,[29] with randomness added in the spike parameters to enhance the QERS effect as explained above. To explore tunability without undue bias a set of 10 simulations with randomized parameters were performed for each of these three structures (structural details can be found in the Supporting Information.[30]) The medium size structure is the same as presented in Supporting Information Figures S4 and S7).[29] As shown in Figure 6b, the far-field scattering peak in air can be tuned over a range of about 200 nm, with the cross section moderately increasing with the overall size of the particle. Figure 6c shows that as the spike length, number, and aspect ratio are increased, the quadrupole moments increase in both strength and breadth. Consistent with our discussions above, larger quadrupole moments result in increased enhancement

factors at 1077 cm^{-1} as shown in Figure 6d. Individual data for the scattering, enhancement, and quadrupole moments are shown in Supporting Information Figure S4 for the medium-sized structure. Supporting Information Figure S7 shows the average of all 6 quadrupole moments, including the weaker $Q_{\alpha\beta}$ modes for the medium-sized structure. These simulations suggest that the optimum QERS cross section can be tailored for particular applications. The combination of tunability with the reproducibility of the QERS enhancement can be extremely useful in biological and sensing applications.

CONCLUSION

These calculations show that heterogeneous substructure in disordered nanoshells is essential to the generation of strong dark quadrupole resonances that are both spectrally and spatially broad. The spectral breadth of the quadrupole resonances allows for effective coupling to both the excitation and the Stokes scattering modes, which results in increased QERS enhancement. Despite the large variations of the value of individual quadrupole moments of disordered nanoshells, the broadening of multiple quadrupoles lead to the emergence of highly reliable Raman enhancement in these nanoshells. This emerging property from added disorder is novel and merits further investigation in other nanoparticle systems. These results show that spiky nanoshells do not need to be perfectly ordered, or sized to be efficient QERS enhancers. In fact, as long as a continuous shell is maintained,[28,29] the added disorder increases the Raman scattering cross section. Furthermore, the disorder-induced spatial breadth allows omnidirectional sensing and effective coupling of many Raman analytes to the local electric field, which is critical in achieving a uniform Raman signal on a single nanoshell level. This differs from most designed dark plasmonic structures, which need to be precisely configured to achieve high enhancement factors,[19] providing a new paradigm for materials design.

METHODS

Spiky nanoshells were synthesized using a recently reported procedure.[27−29] The structure of the nanoshells is shown in Figure 1a. Synthesized nanoshells were placed on a transparent substrate at a concentration suitable for single particle Raman and backscattering measurements. 4-Mercaptobenzoic acid (Figure 1b) was immobilized on the nanoshells as the Raman analyte. A total of 71 individual spiky nanoshells were investigated using an inverted microscope geometry as illustrated in Figure 1c.[38] After all optical measurements, the samples were imaged by SEM (Figure 1e) and compared with backscattering images (Figure 1d) to ensure that only single particle data was included in the analysis. A brief description of the synthesis, sample preparation, single particle backscattering and Raman experiments can be found in the Supporting Information.[30]

Using transmission electron microscopy and scanning electron microscopy (Figure 1a) images of spiky nanoshells,

two model nanoshells were generated for Finite-Difference Time Domain (FDTD) simulations, as described in our previous publications.[28,29] FDTD simulations were performed using Lumerical Solutions, Inc.'s FDTD Solutions software package (versions 8.6 and 8.7). On the basis of experimental variables, two representative structures were modeled (Figure 3a): an ordered nanoshell, with identical spikes placed symmetrically; and a disordered nanoshell, with randomized spike positions, sizes and shapes. The height, cone angle, and tip diameter of all of the spikes are identical in the ordered model and are 58 nm, 60°, and 10 nm, respectively. For the short models, 40 spikes with lengths between 38 and 53 nm, cone angles between 45 and 85° and tips between 2 and 6 nm were used. The disordered model and the medium models were as described above: 60 spikes with randomly chosen spike heights between 50 and 65 nm, tip radii between 2 and 6 nm, and cone angles of 30−75°. The long models were chosen to have 80 spikes with length 58−73 nm, cone angle 15−45°, and tips between 2 and

6 nm in radius. All models have the same 95 nm core size. The parameters for these models were chosen to be consistent with the experimental data. The smooth shell was modeled as gold on polystyrene with inner and outer diameters of 98 and 172 nm, respectively. This produces a gold volume in the smooth shell equal to that in the disordered model. Further simulation details can be found in the Supporting Information.[30]

Conflict of Interest: The authors declare no competing financial interest.

Supporting Information Available: Spiky nanoshell synthesis, optical characterization methods, FDTD simulation methods and spherical harmonic expansions. This material is available free of charge *via* the Internet at http://pubs.acs.org.

REFERENCES AND NOTES

1. Haynes, C. L.; McFarland, A. D.; Van Duyne, R. P. Surface-Enhanced Raman Spectroscopy. *Anal. Chem.* **2005**, *77*, 338–346.
2. Kneipp, K.; Wang, Y.; Kneipp, H.; Perelman, L.; Itzkan, I.; Dasari, R.; Feld, M. Single Molecule Detection Using Surface-Enhanced Raman Scattering (SERS). *Phys. Rev. Lett.* **1997**, *78*, 1667–1670.
3. Dasary, S. S. R.; Singh, A. K.; Senapati, D.; Yu, H.; Ray, P. C. Gold Nanoparticle Based Label-Free SERS Probe for Ultrasensitive and Selective Detection of Trinitrotoluene. *J. Am. Chem. Soc.* **2009**, *131*, 13806–13812.
4. Chang, S.; Ko, H.; Singamaneni, S.; Gunawidjaja, R.; Tsukruk, V. V. Nanoporous Membranes with Mixed Nanoclusters for Raman-Based Label-Free Monitoring of Peroxide Compounds. *Anal. Chem.* **2009**, *81*, 5740–5748.
5. Golightly, R. S.; Doering, W. E.; Natan, M. J. Surface-Enhanced Raman Spectroscopy and Homeland Security: A Perfect Match? *ACS Nano* **2009**, *3*, 2859–2869.
6. Rule, K. L.; Vikesland, P. J. Surface-Enhanced Resonance Raman Spectroscopy for the Rapid Detection of Cryptosporidium Parvum and Giardia Lamblia. *Environ. Sci. Technol.* **2009**, *43*, 1147–1152.
7. Saha, K.; Agasti, S. S.; Kim, C.; Li, X.; Rotello, V. M. Gold Nanoparticles in Chemical and Biological Sensing. *Chem. Rev.* **2012**, *112*, 2739–2779.
8. Huang, P.-J.; Tay, L.-L.; Tanha, J.; Ryan, S.; Chau, L.-K. Single-Domain Antibody-Conjugated Nanoaggregate-Embedded Beads for Targeted Detection of Pathogenic Bacteria. *Chem.—Eur. J.* **2009**, *15*, 9330–9334.
9. Kneipp, J.; Kneipp, H.; Wittig, B.; Kneipp, K. Following the Dynamics of pH in Endosomes of Live Cells with SERS Nanosensors. *J. Phys. Chem. C* **2010**, *114*, 7421–7426.
10. Qian, X.; Peng, X.-H.; Ansari, D. O.; Yin-Goen, Q.; Chen, G. Z.; Shin, D. M.; Yang, L.; Young, A. N.; Wang, M. D.; Nie, S. *In Vivo* Tumor Targeting and Spectroscopic Detection with Surface-Enhanced Raman Nanoparticle Tags. *Nat. Biotechnol.* **2008**, *26*, 83–90.
11. Stiles, P. L.; Dieringer, J. A.; Shah, N. C.; Van Duyne, R. P. Surface-Enhanced Raman Spectroscopy. *Annu. Rev. Anal. Chem.* **2008**, *1*, 601–626.
12. Herzog, J. B.; Knight, M. W.; Li, Y.; Evans, K. M.; Halas, N. J.; Natelson, D. Dark Plasmons in Hot Spot Generation and Polarization in Interelectrode Nanoscale Junctions. *Nano Lett.* **2013**, *13*, 1359–1364.
13. Talley, C. E.; Jackson, J. B.; Oubre, C.; Grady, N. K.; Hollars, C. W.; Lane, S. M.; Huser, T. R.; Nordlander, P.; Halas, N. J. Surface-Enhanced Raman Scattering from Individual Au Nanoparticles and Nanoparticle Dimer Substrates. *Nano Lett.* **2005**, *5*, 1569–1574.
14. Kleinman, S. L.; Sharma, B.; Blaber, M. G.; Henry, A.-I.; Valley, N.; Freeman, R. G.; Natan, M. J.; Schatz, G. C.; Van Duyne, R. P. Structure Enhancement Factor Relationships in Single Gold Nanoantennas by Surface-Enhanced Raman Excitation Spectroscopy. *J. Am. Chem. Soc.* **2013**, *135*, 301–308.
15. Wustholz, K. L.; Henry, A.-I.; McMahon, J. M.; Freeman, R. G.; Valley, N.; Piotti, M. E.; Natan, M. J.; Schatz, G. C.; Van Duyne, R. P. Structure-Activity Relationships in Gold Nanoparticle Dimers and Trimers for Surface-Enhanced Raman Spectroscopy. *J. Am. Chem. Soc.* **2010**, *132*, 10903–10910.
16. Cathcart, N.; Kitaev, V. Multifaceted Prismatic Silver Nanoparticles: Synthesis by Chloride-Directed Selective Growth from Thiolate-Protected Clusters and SERS Properties. *Nanoscale* **2012**, *4*, 6981–6989.
17. Liang, H.; Li, Z.; Wang, W.; Wu, Y.; Xu, H. Highly Surface-Roughened "Flower-like" Silver Nanoparticles for Extremely Sensitive Substrates of Surface-Enhanced Raman Scattering. *Adv. Mater.* **2009**, *21*, 4614–4618.
18. Lim, D.-K.; Jeon, K.-S.; Hwang, J.-H.; Kim, H.; Kwon, S.; Suh, Y. D.; Nam, J.-M. Highly Uniform and Reproducible Surface-Enhanced Raman Scattering from DNA-Tailorable Nanoparticles with 1-nm Interior Gap. *Nat. Nanotechnol.* **2011**, *6*, 452–460.
19. Banholzer, M. J.; Millstone, J. E.; Qin, L.; Mirkin, C. A. Rationally Designed Nanostructures for Surface-Enhanced Raman Spectroscopy. *Chem. Soc. Rev.* **2008**, *37*, 885–897.
20. Xu, H.; Käll, M. Polarization-Dependent Surface-Enhanced Raman Spectroscopy of Isolated Silver Nanoaggregates. *ChemPhysChem* **2003**, *4*, 1001–1005.
21. Ahmed, A.; Gordon, R. Directivity Enhanced Raman Spectroscopy Using Nanoantennas. *Nano Lett.* **2011**, *11*, 1800–1803.
22. Haynes, C. L.; Van Duyne, R. P. Plasmon-Sampled Surface-Enhanced Raman Excitation Spectroscopy. *J. Phys. Chem. B* **2003**, *107*, 7426–7433.
23. Wang, H.; Halas, N. J. Mesoscopic Au "Meatball" Particles. *Adv. Mater.* **2008**, *20*, 820–825.
24. Messinger, B. J.; Von Raben, K. U.; Chang, R. K.; Barber, P. W. Local Fields at the Surface of Noble-Metal Microspheres. *Phys. Rev. B* **1981**, *24*, 649–657.
25. Zhou, F.; Li, Z.-Y.; Liu, Y.; Xia, Y. Quantitative Analysis of Dipole and Quadrupole Excitation in the Surface Plasmon Resonance of Metal Nanoparticles. *J. Phys. Chem. C* **2008**, *112*, 20233–20240.
26. Hermoso, W.; Alves, T. V.; Ornellas, F. R.; Camargo, P. H. C. Comparative Study on the Far-Field Spectra and near-Field Amplitudes for Silver and Gold Nanocubes Irradiated at 514, 633 and 785 nm as a Function of the Edge Length. *Eur. Phys. J. D* **2012**, *66*, 1–11.
27. Sanchez-Gaytan, B. L.; Park, S.-J. Spiky Gold Nanoshells. *Langmuir* **2010**, *26*, 19170–19174.
28. Sanchez-Gaytan, B. L.; Swanglap, P.; Lamkin, T. J.; Hickey, R. J.; Fakhraai, Z.; Link, S.; Park, S.-J. Spiky Gold Nanoshells: Synthesis and Enhanced Scattering Properties. *J. Phys. Chem. C* **2012**, *116*, 10318–10324.
29. Sanchez-Gaytan, B. L.; Qian, Z.; Hastings, S. P.; Reca, M. L.; Fakhraai, Z.; Park, S.-J. Controlling the Topography and Surface Plasmon Resonance of Gold Nanoshells by a Templated Surfactant-Assisted Seed Growth Method. *J. Phys. Chem. C* **2013**, *117*, 8916–8923.
30. See Supporting Information.
31. Buckingham, A. D. Permanent and Induced Molecular Moments and Long-Range Intermolecular Forces. *Adv. Chem. Phys.* **1967**, *12*, 107–142.
32. Lombardi, J. R.; Birke, R. L. A Unified Approach to Surface-Enhanced Raman Spectroscopy. *J. Phys. Chem. C* **2008**, *112*, 5605–5617.
33. Weitz, D. a.; Garoff, S.; Gersten, J. I.; Nitzan, A. The Enhancement of Raman Scattering, Resonance Raman Scattering,

and Fluorescence from Molecules Adsorbed on a Rough Silver Surface. *J. Chem. Phys.* **1983**, *78*, 5324–5338.

34. Papas, C. H. *Theory of Electromagnetic Wave Propagation*; Dover Publications, Inc.: New York, 1988; p 82.

35. Coenen, T.; Bernal Arango, F.; Femius Koenderink, A.; Polman, A. Directional Emission from a Single Plasmonic Scatterer. *Nat. Commun.* **2014**, *5*, 3250.

36. Albrecht, A. C.; Hutley, M. C. On the Dependence of Vibrational Raman Intensity on the Wavelength of Incident Light. *J. Chem. Phys.* **1971**, *55*, 4438–4443.

37. Hao, F.; Nehl, C. L.; Hafner, J. H.; Nordlander, P. Plasmon Resonances of a Gold Nanostar. *Nano Lett.* **2007**, *7*, 729–732.

38. Slaughter, L.; Chang, W.-S.; Link, S. Characterizing Plasmons in Nanoparticles and Their Assemblies with Single Particle Spectroscopy. *J. Phys. Chem. Lett.* **2011**, *2*, 2015–2023.